Transport Phenomena and Keyhole Dynamics during Pulsed Laser Welding

Jun Zhou
Department of Mechanical and Aerospace
Engineering,
University of Missouri-Rolla,
229 Mechanical Engineering,
1870 Miner Circle,
Rolla, MO 65409
e-mail: jzhou@umr.edu

Hai-Lung Tsai
Department of Mechanical and Aerospace
Engineering,
University of Missouri-Rolla,
122 Mechanical Engineering Annex,
1870 Miner Circle,
Rolla, MO 65409
e-mail: tsai@umr.edu

Pei-Chung Wang
R & D Center,
General Motors Corporation,
Warren, MI 48090
e-mail: Pei-chung.wang@gm.com

Numerical and experimental studies were conducted to investigate the heat transfer, fluid flow, and keyhole dynamics during a pulsed keyhole laser welding. A comprehensive mathematical model has been developed. In the model, the continuum formulation was used to handle solid phase, liquid phase, and mushy zone during melting and solidification processes. The volume-of-fluid method was employed to handle free surfaces. The enthalpy method was used for latent heat. Laser absorptions (Inverse Bremsstrahlung and Fresnel absorption) and thermal radiation by the plasma in the keyhole were all considered in the model. The results show that the recoil pressure is the main driving force for keyhole formation. Combining with the Marangoni shear force, hydrodynamic force, and hydrostatic force, it causes very complicated melt flow in the weld pool. Laser-induced plasma plays twofold roles in the process: (1) to facilitate the keyhole formation at the initial stage and (2) to block the laser energy and prevent the keyhole from deepening when the keyhole reaches a certain depth. The calculated temperature distributions, penetration depth, weld bead size, and geometry agreed well with the corresponding experimental data. The good agreement demonstrates that the model lays a solid foundation for the future study of porosity prevention in keyhole laser welding. [DOI: 10.1115/1.2194043]

Keywords: laser welding, heat transfer, fluid flow, modeling, free surface, keyhole, computational, VOF

1 Introduction

Welding with lasers is characterized by creating a keyhole inside the molten metal. A high-energy-density beam vaporizes the workpiece during the welding process to form a deep hole, which is called the keyhole. The keyhole increases the coupling of laser energy into the workpiece, resulting in a weld with high depth-to-width ratio and a narrow heat-affected zone. However, porosity is easy to find in laser weld, which is a major defect of laser welding. Since the porosity formation and weld quality depend on the heat transfer and the melt flow during the formation and collapse of the keyhole, it is necessary to study the detailed transport phenomena during the welding process.

So far, most of the models investigating the keyhole formation and collapse mechanisms can be divided into two categories, one based on the vaporization approach and the other based on recoil pressure research [1]. The vaporization model assumed that there is a balance between the sum of recoil pressure and vapor pressure in the keyhole and the sum of surface tension and hydrostatic pressure. It fails to describe the process of keyhole formation and predicts lower values of melt velocity as compared with experimental results [2]. The second type of vaporization keyhole model [3] assumes that the keyhole is stabilized and held open when the vaporization rate is equal to the mass flow rate of molten metal coming into the keyhole due to hydrostatic pressure. Although this type of model can be used to study the transient behavior of short-duration spot welding, the predicted behavior for a longer time process does not coincide with experimental data of keyhole dynamics [2]. The model based on recoil pressure approach assumes that the recoil pressure acts as a driving force for melt flow and keyhole formation. The recoil pressure, acting toward the metal, is a kind of reaction force, as opposed to the action force caused by

the sudden "burst" of vapor from the metal when a laser beam impinges onto it. Klemens [4] proposed a model in which the motion of the melt was a significant factor for keyhole support. Allmen and Blatter [5] proposed that a Knudsen layer was formed above the molten region and extended beyond the keyhole surface for a few mean free paths. A discontinuity in temperature, pressure, and density occurred across the evaporation front, with the flow of hot vapor propagating as a shock wave outward. Solana et al. [6] further developed a mathematical model for the ablation process. Clucas et al. [7] developed a mathematical model for the keyhole welding process by suggesting a pressure and energy balance at the keyhole walls. The pressure balance was described in terms of surface tension, recoil pressure, and hydrodynamic pressure inside the keyhole. The energy was balanced between the laser light absorption energy and the heat by a conduction and ablation process.

During the keyhole formation process, the melt flow was very complex and unstable, which was considered to be the main cause for porosity formation [8]. Chen and Bos [9] investigated the role of melt flow in determining the operating characteristics of deep keyhole welding and explained why keyhole formation was considerably easier under a reduced environment pressure. Ducharme et al. [10] developed an integrated keyhole and weld pool model for thin metal sheets welding. The predicted shape of weld pool by this model agreed well with the experiment. Sudnik et al. [11] further analyzed the three driving forces of melt flow, including the force resulting from temperature-dependent surface tension, the friction force of metal vapor escaping from the capillary, and the movement of capillary relative to the workpiece. The shape of keyhole and the melt flow velocity were both calculated numerically.

Laser-induced plasma was presented as a result of ablation vapor from the keyhole wall, which was heated up to be partially ionized under the laser radiation. Laser-induced plasma is considered to be an important factor affecting keyhole behavior. Kapadia et al. [12] thought the high vapor temperature required for plasma

---

Fig. 1 Experimental setup and schematic sketch of static key-hole laser welding process

2.1 Metal Zone Simulation

2.1.1 Governing Equations. The governing differential equations used to describe heat and mass transfer and fluid flow in a cylindrical coordinate (r-z system) given by Chiang and Tsai [18] are modified and used in the current study.

Continuity

$$\frac{\partial}{\partial t}(\rho) + \nabla \cdot (\rho V) = 0 \tag{1}$$

Momentum

$$\frac{\partial}{\partial t}(\rho u) + \nabla \cdot (\rho V u) = \nabla \cdot \left(\mu_l \frac{\rho}{\rho_l} \nabla u \right) - \frac{\partial p}{\partial r} - \frac{u_l}{K} \frac{\rho}{\rho_l}(u - u_s)$$
$$- \frac{C\rho^2}{K^{0.5}\rho_l}|u - u_s|(u - u_s) - \nabla \cdot (\rho f_s f_l V_r u_r)$$
$$+ \nabla \cdot \left[\mu_s u \nabla \left(\frac{\rho}{\rho_l} \right) \right] \tag{2}$$

$$\frac{\partial}{\partial t}(\rho v) + \nabla \cdot (\rho V v) = \rho g + \nabla \cdot \left(\mu_l \frac{\rho}{\rho_l} \nabla v \right) - \frac{\partial p}{\partial z} - \frac{u_l}{K} \frac{\rho}{\rho_l}(v - v_s)$$
$$- \frac{C\rho^2}{K^{0.5}\rho_l}|v - v_s|(v - v_s) - \nabla \cdot (\rho f_s f_l V_r v_r)$$
$$+ \nabla \cdot \left[\mu_s v \nabla \left(\frac{\rho}{\rho_l} \right) \right] + \rho g \beta_T(T - T_0) \tag{3}$$

Energy

$$\frac{\partial}{\partial t}(\rho h) + \nabla \cdot (\rho V h) = \nabla \cdot \left(\frac{k}{c_p} \nabla h \right) - \nabla \cdot \left(\frac{k}{c_p} \nabla (h_s - h) \right)$$
$$- \nabla \cdot [\rho(V - V_s)(h_l - h)] \tag{4}$$

The physical meaning of each term appearing in the above equations can be found in Ref. [18]. In Eqs. (1)–(4), the continuum density, specific heat, thermal conductivity, solid mass fraction, liquid mass fraction, velocity, and enthalpy are defined in Ref. [20].

2.1.2 Tracking of Free Surfaces. The algorithm of volume-of-fluid is used to track the dynamic free surface [17]. The fluid configuration is defined by a volume of fluid function $F(r, z, t)$, which tracks the location of free surface. The function F takes the value of one for the cell full of fluid and the value of zero for the empty cell. Cells with F values between zero and one are partially filled with fluid and identified as surface cells. The function F is governed by

$$\frac{dF}{dt} = \frac{\partial F}{\partial t} + (V \cdot \nabla)F = 0 \tag{5}$$

2.1.3 Boundary Conditions. The corresponding boundary conditions of the metal zone simulation are divided into five categories according to their positions, as shown in Fig. 1.

Top surface inside the keyhole (AE in Fig. 1). For cells containing free surface, that is, cells that contain fluid but have one or more empty neighbors, in the direction normal to the free surface, the following pressures condition must be satisfied [21]

$$p = p_r + p_\sigma \tag{6}$$

where p is the pressure at the free surface in a direction normal to the local free surface, p_σ is surface tension, and p_r is recoil pressure. p_σ can be calculated as [20]

$$p_\sigma = \kappa\gamma \tag{7}$$

κ is the free surface curvature, given by [20]

Introduction (left column continued)

ignition was due to the small droplet radius and the presence of surface tension around droplet. Farson and Kim [13] simulated laser-induced evaporation and plume formation. They pointed out that a stable plume could be formed when the material surface irradiance was reduced. For the welding process at a lower flow rate of argon assistant gas, the Inverse Bremsstrahlung (IB) absorption in the plasma and the heating of the keyhole walls by the heat transfer from plasma could not be neglected [14]. Solana and Negro [15] analyzed the effect of multiple reflections on the keyhole wall, assuming the keyhole was axisymmetrical and that the keyhole wall acted as a free boundary. Metzbower [16] thought the absorption of laser energy in the keyhole was a function of laser frequency, welded material, and the temperature of the vapor.

Despite the large number of investigations referenced above, a comprehensive model of keyhole formation process that includes the simulations of temperature field, pressure balance, melt flow, free surface, laser-induced plasma, and multiple reflections has not yet been found. In this study, the transient keyhole formation and collapse process and weld pool dynamics during a pulsed laser welding has been investigated. The recoil pressure acts as a driving force for melt flow, which is considered as the primary influence factor for keyhole formation. The laser-induced plasma acts as an important role affecting keyhole behavior once it occurs.

2 Mathematical Models

Figure 1 shows the schematic sketch of a pulsed keyhole laser welding. A finite difference model employing the volume-of-fluid (VOF) technique [17] and the continuum formulation [18] is used to calculate the momentum and energy transport in the weld pool. The VOF technique can handle a transient deformed weld pool surface, while the continuum formulation can handle fusion and solidification for the liquid region, the mush zone, and the solid region. Plasma in the keyhole can be treated as the vapor of the weld material. Although the velocity and pressure change dramatically across the Knudsen layer, the generic translation vapor flow along the keyhole is neglected [14]. Meanwhile, the pressure along the keyhole can also be considered to be approximately constant [19] and will be comparable to the atmospheric pressure.

$$\kappa = -\left[\mathbf{\nabla} \cdot \left(\frac{\mathbf{n}}{|\mathbf{n}|}\right)\right] = \frac{1}{|\mathbf{n}|}\left[\left(\frac{\mathbf{n}}{|\mathbf{n}|} \cdot \mathbf{\nabla}\right)|\mathbf{n}| - (\mathbf{\nabla} \cdot \mathbf{n})\right] \quad (8)$$

where $\mathbf{n}$ is the vector normal to the local free surface. For a pseudo-binary Fe–S system, the surface tension coefficient γ can be calculated as the function of temperature T and sulfur concentration f^α [22]

$$\gamma = 1.943 - 4.3 \times 10^{-4}(T - 1723) - RT \times 1.3$$
$$\times 10^{-8}\ln\left[1 + 0.00318 f^\alpha \exp\left(\frac{1.66 \times 10^8}{RT}\right)\right] \quad (9)$$

The temperature-dependent Marangoni shear stress on the free surface in the direction tangential to the local surface is given by [23]

$$\tau_{\mathbf{s}} = \mu_l \frac{\partial(\mathbf{V} \cdot \mathbf{s})}{\partial \mathbf{n}} = \frac{\partial \gamma}{\partial T}\frac{\partial T}{\partial \mathbf{s}} \quad (10)$$

Calculation of the evaporation-induced recoil pressure p_r is complicated by the existence of a Knudsen layer over the vaporizing surface. Based on Knight's model [24], the recoil pressure can be given by [25]

$$p_r = A P_s(T_w) = A B_0/\sqrt{T_w} \exp(-U/T_w) \quad (11)$$

where A is the numerical coefficient and B_0 is a vaporization constant. The coefficient A depends on the ambient pressure and its value varies from 0.55 for evaporation in the vacuum to 1 for the case of evaporation under a high ambient pressure. For practical values of the ambient pressure, the coefficient A is close to its minimal value of 0.55. B_0 is at the value of 1.78×10^{10}. T_w is the temperature of the surface liquid metal. The parameter U is defined as [25]

$$U = M_a H_v/(N_A k_B) \quad (12)$$

where M_a is atomic mass, H_v is the latent heat of evaporation, N_A is Avogadro's number, and k_B is Boltzmann's constant.

The energy on the top free surface is balanced among the laser radiation, plasma-keyhole wall radiation, the heat dissipation through convection, and metal vaporization. In general, since the velocity of plume along the surface is zero [14], the heat loss due to convection is omitted. The energy balance can be given by the following formula

$$k\frac{\partial T}{\partial \mathbf{n}} = q_{laser} + q_{rad} - q_{evap} \quad (13)$$

In this study, the liquid/vapor evaporation model is used due to the low intensity of laser radiation. Assuming the vaporization mechanism is surface vaporization, the heat loss due to evaporation can be given as [26]

$$q_{evap} = W H_v \quad (14)$$

$$W = n_l\left(\frac{k_B T_l}{2\pi m_a}\right)^{0.5}\exp\left(-\frac{H_v}{k_B T_l}\right) - \theta_s n_v\left(\frac{k_B T_v}{2\pi m_a}\right)^{0.5} \quad (15)$$

where T_l is the liquid surface temperature, m_a is the atom mass, n_l and n_v are the number of atoms per unit volume for liquid and vapor, respectively, and H_v and T_v represent latent heat of vaporization and temperature, respectively. θ_s denotes the probability that a vapor atom returning to the liquid surface from equilibrium conditions at the edge of the discontinuity layer manages to penetrate this layer to finally be absorbed on the liquid surface, which is in the range from 15% to 20%.

The laser heat flux q_{laser} comes from the Fresnel absorption of the incident intensity directly from the laser beam plus the incident intensity from the multiple reflections:

$$q_{laser} = I_0(r,z)(\mathbf{I}_0 \cdot \mathbf{n}_0)\alpha_{Fr}(\varphi_0) + \sum_{m=1}^{n} I_m(r,z)(\mathbf{I}_m \cdot \mathbf{n}_m)\alpha_{Fr}(\varphi_m) \quad (16)$$

$$\alpha_{Fr}(\varphi) = 1 - \frac{1}{2}\left(\frac{1 + (1 - \varepsilon\cos\varphi)^2}{1 + (1 + \varepsilon\cos\varphi)^2} + \frac{\varepsilon^2 - 2\varepsilon\cos\varphi + 2\cos^2\varphi}{\varepsilon^2 + 2\varepsilon\cos\varphi + 2\cos^2\varphi}\right) \quad (17)$$

where φ is the angle of incident light with the normal of keyhole surface, n is the total number of incident light from multiple reflections, $\mathbf{I}$ is the unit vector along the laser beam radiation direction, and $\mathbf{n}$ is the unit vector normal to the free surface. ε is a material-dependent coefficient. In CO_2 laser welding of mild steel, $\varepsilon = 0.2$ is used. $I_0(r,z)$ and $I_m(r,z)$ are the incident intensity from the laser beam and mth multiple reflection at the keyhole surface, respectively, which are given as

$$I_0(r,z) = I_c(r,z)\exp\left(-\int_0^{s_0} K_{pl}ds\right) \quad (18)$$

$$I_m(r,z) = I_r(r,z)\exp\left(-\int_0^{s_m} K_{pl}ds\right) \quad (19)$$

$$I_r(r,z) = I_0(r,z)(1 - \alpha_{Fr}) \quad (20)$$

where $I_c(r,z)$ stands for the collimated incident laser beam intensity, $I_{r,m}(r,z)$ is the reflected laser beam intensity at mth reflections, $\int_0^z K_{pl}dz$ and $\int_0^{s_m} K_{pl}ds$ are the optical thickness of the laser transportation path, respectively, for the first incident and multiple reflections, K_{pl} is the plasma absorption coefficient due to the IB absorption [21]

$$K_{pl} = \frac{n_e n_i Z^2 e^6 2\pi}{6\sqrt{3}m\varepsilon_0^3 ch\omega^3 m_e^2}\left(\frac{m_e}{2\pi k_B T_e}\right)^{0.5}\left[1 - \exp\left(-\frac{\omega}{k_B T_e}\right)\right]\bar{g} \quad (21)$$

where Z is the average ionic charge in the plasma, ω is the angular frequency of the laser radiation, ε_0 is dielectric constant, n_e and n_i are particle densities of electrons and ions, respectively, h is Planck's constant, m_e is the electron mass, T_e is the excitation temperature, c is the speed of light, and $\bar{g}$ is the quantum mechanical Gaunt factor. For weakly ionized plasma in the keyhole, the Saha equation [21] can be used to calculate the densities of plasma species

$$\frac{n_e n_i}{n_0} = \frac{g_e g_i}{g_0}\frac{(2\pi m_e k_B T_e)^{1.5}}{h^3}\exp\left(-\frac{E_i}{k_B T_e}\right) \quad (22)$$

where g_e, g_i, and g_0 are the degeneracy factors for electrons, ions, and neutral atoms, respectively, and E_i is the ionization potential for the neutral atoms in the gas. Assuming the laser intensity distribution is ideal Gaussian-like, $I_c(r,z)$ can be calculated as [27]

$$I_c(r,z) = I_0\left(\frac{r_f}{r_{f0}}\right)^2\exp\left(-\frac{2r^2}{r_f^2}\right) \quad (23)$$

where r_f is the beam radius, r_{f0} is the beam radius at the focal position, and I_0 is the peak intensity.

In laser welding, the keyhole surface temperature is much lower than that of the plume, so that the radiation and emission of surface can be omitted. Then q_{rad} can be simplified as

$$q_{rad} = \varepsilon\sigma(T_{pl}^4 - T^4) \quad (24)$$

Here, T_{pl} is the temperature of the plasma.

Top surface outside the keyhole (AB in Fig. 1). The boundary condition on the top surface outside the keyhole is similar to that

inside the keyhole. The differences lie in the absence of plasma and multiple reflections. As shown in Fig. 1, there is a shielding gas flow above the base metal, which means that any plasma outside the keyhole will be blown away. Thus, Eq. (16) can be written as

$$q_{laser} = I_c(r,z)\alpha_{Fr}\cos\varphi \tag{25}$$

Since there is no plasma and the temperature of shielding gas is much lower than that of the metal surface, the radiation heat flux can be given as

$$q_{rad} = -\varepsilon\sigma(T^4 - T_\infty^4) \tag{26}$$

Here, T_∞ is the ambient temperature. Moreover, since there is a shielding gas flow over the surface, the convection term cannot be omitted. It can be given as

$$q_{conv} = h(T - T_\infty) \tag{27}$$

Side surface (BC in Fig. 1).

$$-k\frac{\partial T}{\partial r} = q_{conv} \tag{28}$$

$$u = 0, \quad v = 0 \tag{29}$$

Bottom surface (CD in Fig. 1).

$$-k\frac{\partial T}{\partial z} = q_{conv} \tag{30}$$

$$u = 0, \quad v = 0 \tag{31}$$

Symmetrical axis (DE in Fig. 1).

$$\frac{\partial T}{\partial r} = 0 \tag{32}$$

$$u = 0, \quad \frac{\partial v}{\partial r} = 0 \tag{33}$$

2.2 Plasma Zone Simulation.

2.2.1 Governing Equations. In current study, the metal vapor in the keyhole is assumed to be a compressible, inviscous ideal gas. Since the heat production by viscous dissipation is rather small in laser welding, the energy equation can be simplified as [28]

$$\frac{\partial}{\partial t}(\rho_{pl}h_{pl}) = \nabla\cdot\left(\frac{k_{pl}}{c_{pl}}\nabla h_{pl}\right) + K_{pl}I_c\exp\left(-\int_0^s K_{pl}ds\right)$$
$$+ \sum_{m=1}^{n} K_{pl}I_{r,m}(r,z)\exp\left(-\int_0^{s_m} K_{pl}ds\right) \tag{34}$$

where h_{pl} and ρ_{pl} represent the enthalpy and density of the plasma, respectively, k_{pl} and c_{pl} represent the thermal conductivity and specific heat of the plasma, respectively, s is the penetration depth of laser light in plasma, and K_{pl} denotes the plasma laser light IB absorption coefficient. When an intense laser pulse interacts with the vapor in the keyhole, a significant amount of laser radiation is absorbed by the ionized particles through IB absorption. For the laser-induced plasma inside the keyhole, the scattering effect is not significant compared with the absorbing and emitting effects. For simplicity, the plasma is assumed to be an absorbing-emitting medium and the laser intensity is exponentially attenuated inside the keyhole plasma.

2.2.2 Boundary Conditions

Bottom surface inside the keyhole (EA in Fig. 1). Close to the liquid wall inside the keyhole, there is the so-called Knudsen layer

where vaporization of material takes place. The vapor temperature across the Knudsen layer is discontinuous, which can be calculated by [24]:

$$\frac{T_K}{T_L} = \left[\sqrt{1 + \pi\left(\frac{\gamma-1}{\gamma+1}\frac{m}{2}\right)^2} - \sqrt{\pi}\frac{\gamma-1}{\gamma+1}\frac{m}{2}\right]^2 \tag{35}$$

$$m = M_k\sqrt{\frac{2}{\gamma}} \tag{36}$$

where T_K is the temperature outside of the Knudsen layer, T_L is the liquid surface temperature adjacent to the Knudsen layer, M_k is Mach number at the outer of the Knudsen layer, and γ is the ratio of specific heat. The value of m depends on the gas dynamics of the vapor flow away from the surface. Since it is assumed that there is no shock wave outside the Knudsen layer, the gas temperature outside the Knudsen layer is used as the boundary temperature. Thus, the boundary condition is given as [29]

$$T_{pl} = T_K \tag{37}$$

Top surface outside the keyhole (FA in Fig. 1).

$$T_{pl} = T_\infty \tag{38}$$

Symmetrical axis (EF in Fig. 1).

$$\frac{\partial T_{pl}}{\partial r} = 0 \tag{39}$$

3 Numerical Method

In computation, the calculation of transport equations in metal zone and plasma zone are coupled. That is, the simulations of metal zone and plasma zone provide boundary conditions for each other. However, there are large spatial and physical differences between them. For a compromise between the result convergence and calculation time, different time resolution were used for these simulations. The governing equations (Eqs. (1)–(5) and (34)), all related supplemental equations and boundary conditions are solved through the following iterative scheme:

(1) Equations (1)–(4) are solved iteratively to obtain velocity, pressure, and temperature distributions under the associated boundary conditions for the metal zone.
(2) Equation (34) is solved iteratively to obtain the temperature field of the plasma in the keyhole under the associate boundary conditions.
(3) Iteration between steps (1) and (2).
(4) Solve VOF algorithm Eq. (5) to obtain the new domain for the metal zone and the plasma zone.
(5) Update the boundary conditions for the metal zone and the plasma zone.
(6) Advance to the next time step until the desired time is reached.

The technique for solving the partial differential equations is given by Wang and Tsai [20]. Following the Marker-And-Cell (MAC) scheme, the r and z velocity components are located at cell face centers on lines of constants r and z, respectively, while the pressure, VOF function, temperature, and absorbed laser flux are located at cell centers. Since the temperature and pressure field change more dramatically near the keyhole, a nonuniform grid system with 202×252 points is used for the total computational domain of $5.0 \text{ mm} \times 6.25 \text{ mm}$, in which smaller grids are arranged near the keyhole and larger grids for other parts. Due to the axis symmetry of the domain, only half of the grid points were used in the actual calculation. Calculations were executed on the DELL OPTIPLEX GX270 workstations with LINUX-REDHAT

9.0 OS and took 6 h of CPU time to simulate about 100 ms of real-time welding. The average time step is 10^{-4} s and the smallest time step is about 10^{-6} s.

4 Experimental Method

Bead-on-plate welding experiments were conducted by GM R&D engineers using a TRUMPF HL 4006D Nd:YAG laser system. The maximum output power of the laser at the workpiece is 4.0 kW and the wavelength is 1064 nm. The experimental setup is similar to that shown in Fig. 1. Plate specimens (40.0 mm × 3.0 mm) made of 304 standard steels were chemically cleaned and degreased. Argon was used as the protecting gas, the flow rate of which was 20 l/min. The laser beam pulse shape, modulation, and ramping are programmable or can be set externally. The diameter of the laser beam at the focus plane is 500 μm and the focus plane is on the top surface of the workpiece. The welding parameters, such as laser power, on-time duration, and beam diameter, were monitored and used in the mathematical model. Thermal profiles were recorded using K-type thermocouples welded to the symmetrical "A" (2 mm right to the laser beam center) and "B" (2 mm left to the laser beam center) locations underside of the coupon. Macroscopic analysis performed under stereoscopes and optical microscopes. An image acquisition system including a digital camera, a microscope, and a computer was used to capture and store the images. Adobe Photoshop® and Image Processing Tool Kit® software were used for the processing of the sample images. The experiments were conducted for various laser power levels and on-time durations. The weld penetration, width, and bead geometry, and temperature profiles at "A" and "B" locations for each case were measured.

5 Results and Discussion

The thermophysical properties and welding conditions used in the present study are summarized in Table 1. The following welding conditions are assumed in the model: laser power at the focus is 2.5 kW, the radius at focus is 0.25 mm, and the laser beam energy is in the Gaussian distribution. The laser power is assumed to increase from 0 to 2.5 kW in 1.0 ms and the pulse duration is 14.0 ms. The divergence of the laser beam is assumed to be negligible for a 3.0 mm metal thickness. The complete sequence of the keyhole formation and collapse and the associated weld pool fluid flow are calculated.

5.1 Keyhole Formation. Figure 2 shows the keyhole formation process. The corresponding temperature and velocity distributions are given, respectively, in Figs. 3 and 4. At the initial stage ($t < 1.8$ ms), the laser energy is mainly used to heat up the base metal. As the temperature of the base metal increases, a small weld pool starts to appear under the laser beam. When the laser power reaches 2.5 kW at $t = 1.0$ ms, the laser-induced recoil pressure starts to push down the molten metal under the laser beam. Since it takes time to accelerate the molten metal from a static condition, and the weld pool is thin at this time, the surface of the weld pool is nearly flat. Only part of the laser energy is absorbed by the metal via Fresnel absorption; the rest is reflected away. Heat conduction is the major heat transfer mode at this stage.

As the laser light continues to radiate, the temperature of the weld pool surface increases, as shown in Fig. 3. The large temperature difference along the free surface of the weld pool due to the Gaussian distribution of laser power leads to a high temperature-dependent Marangoni shear stress. As shown in Fig. 5, the gradient of surface tension coefficient on temperature change $\partial\gamma/\partial T$ is negative when T is above 2150 K. Since the temperature on the weld pool surface under laser radiation is more than 2150 K and the temperature gradient along the surface from the center to the outside of the weld pool $\partial T/\partial \mathbf{S}$ is negative, the temperature-dependent Marangoni shear stress is positive along the weld pool surface, which drives the fluid to flow outwards. In

Table 1 Thermophysical properties of 304 stainless steel and process parameters

Nomenclature	Value
Specific heat of solid phase c_s (J kg^{-1} K^{-1})	700
Specific heat of liquid phase c_l (J kg^{-1} K^{-1})	780
Thermal conductivity of solid phase k_s (W m^{-1} K^{-1})	22
Thermal conductivity of liquid phase k_l (W m^{-1} K^{-1})	22
Density of solid phase ρ_s (kg m^{-3})	7200
Density of liquid phase ρ_l (kg m^{-3})	6900
Dynamic viscosity μ_l (kg m^{-1} s^{-1})	0.006
Latent heat of fusion H (J kg^{-1})	2.47×10^5
Solidus temperature T_s (K)	1670
Liquidus temperature T_l (K)	1727
Boiling temperature T_v (K)	3375
Latent heat of vaporization H_v (J kg^{-1})	6.34×10^6
Laser power P (kW)	2.5
Laser beam radius at focus r_{f0} (mm)	0.25
Laser beam radius r_f (mm)	0.25
Substrate initial temperature T_0 (K)	300
Surrounding temperature T_{gas} (K)	300
Ambient temperature T_∞ (K)	300
Thickness of substrate metal H_b (mm)	3.0
Radius of substrate metal R_b (mm)	20.0
Substrate sulfur concentration C_s (ppm)	100
Atmospheric pressure P_{atm} (Pa)	1.013×10^5
Gas constant R (J kg^{-1} mole^{-1})	8.3×10^3
Average ionic charge in the plasma Z	1
Angular frequency of the laser radiation ω (rad s^{-1})	1.78×10^{14}
Quantum mechanical Gaunt factor $\bar{g}$	1.5
Excitation temperature T_e (K)	9×10^3
Degeneracy factors for ions g_i	30
Degeneracy factors for neutral atoms g_0	25
Degeneracy factors for electrons g_e	30
Speed of light c (m s^{-1})	3×10^8
Boltzmann's constant k_B (J K^{-1})	1.38×10^{-23}
Planck's constant h (J s)	6.625×10^{-34}

the surface area where temperature is below 2150 K, surface tension coefficient gradient will change to be a positive value. Since the temperature gradient is still negative, the Marangoni shear stress forces the liquid metal to flow inwards. A crater is then formed at some point of the weld pool where the temperature is above 2150 K, as shown in Fig. 2. Moreover, higher surface temperature leads to higher recoil pressure, which pushes the liquid metal under laser radiation downwards quickly. As shown in Fig. 2, although the liquid-solid interface keeps moving downwards, the liquid region of the weld pool under laser radiation remains only as a thin layer because the strong recoil pressure squeezes the liquid metal to flow outwards. Under the hydrodynamic force and the Marangoni shear stress, this squeezed liquid metal flows upwards along the keyhole wall which facilitates the formation of a crater. As the surface level moves down and the crater level increases, a keyhole is formed in the weld pool at $t = 6.0$ ms.

5.2 The Effects of Laser-Induced Plasma and Multiple Reflections. Once the keyhole comes into being, as shown in Fig. 2 at $t = 6.0$ ms, some metal vapor will be trapped inside it. The incoming laser beam interacts with this metal vapor and part of laser energy is absorbed by it. Since the heat capacity of the vapor is rather low, the temperature of the vapor increases very quickly. When the temperature of the vapor exceeds around 8000 K [15], laser-induced plasma will be formed by the ionization process. The physical properties of plasma are quite different from that of the prior vapor, which absorbs more laser energy through the IB absorption process.

The laser-induced plasma plays twofold roles in keyhole formation. As shown in Fig. 6, the coefficient of the IB absorption increases with the increase of plasma temperature. Hence, once
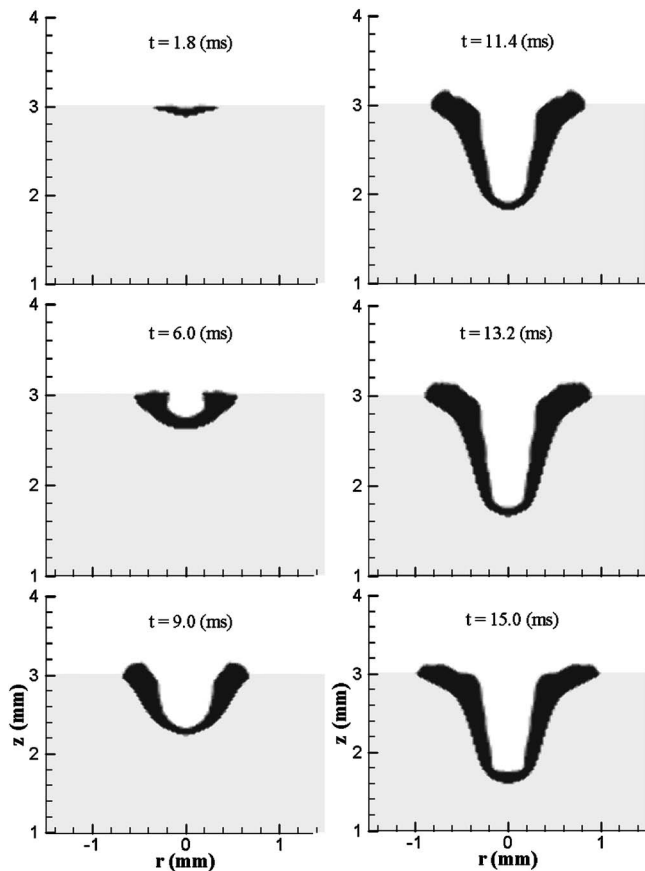
Fig. 2 A sequence of liquid metal evolution during the keyhole formation process

Fig. 3 The corresponding temperature distributions for the case shown in Fig. 2

plasma comes into being, its temperature will increase very quickly, as indicated in Fig. 3. This hot plasma separates the keyhole wall from the cold shielding gas, which reduces the heat loss from the keyhole wall to the surroundings. Moreover, the hot plasma heats up the surrounding keyhole wall via radiation. This facilitates the temperature increase on the keyhole wall when the depth of keyhole is not large. As shown in Fig. 3, the temperature on the keyhole wall under laser radiation keeps increasing. Therefore, the recoil pressure becomes stronger accordingly, which helps the depth of keyhole grow very quickly. As shown in Fig. 7, the drilling speed increases quickly once the keyhole appears, and maintains the value for the time between $t=6.0$ ms and $t=10.4$ ms.

When the plasma temperature is above 10,000 K, as shown in Fig. 6, the IB absorption coefficient decreases with the increasing plasma temperature. Although the coefficient of the IB absorption decreases with the small increase of plasma temperature, the travel length of laser light increases with the increasing keyhole depth, the overall effect of the plasma absorption becomes more and more remarkable, and it will block more percentage of the laser energy to reach the keyhole bottom wall. Meanwhile, the temperature of plasma only increases a little. The heat radiation from the plasma also increases a little correspondingly. Thus, the blocking effect on laser light becomes more and more dominant, which eventually will make the plasma become a negative factor for keyhole depth increase at certain time. As shown in Fig. 7, the keyholing speed drops quickly after $t=11.0$ ms.

The formation of the keyhole also enhances the laser light absorption through a mechanism called multiple reflections. As shown in Fig. 2, the surface of the weld pool is nearly flat at the beginning. Once laser light irradiates the flat surface, only part of the energy is absorbed by the surface via the Fresnel absorption
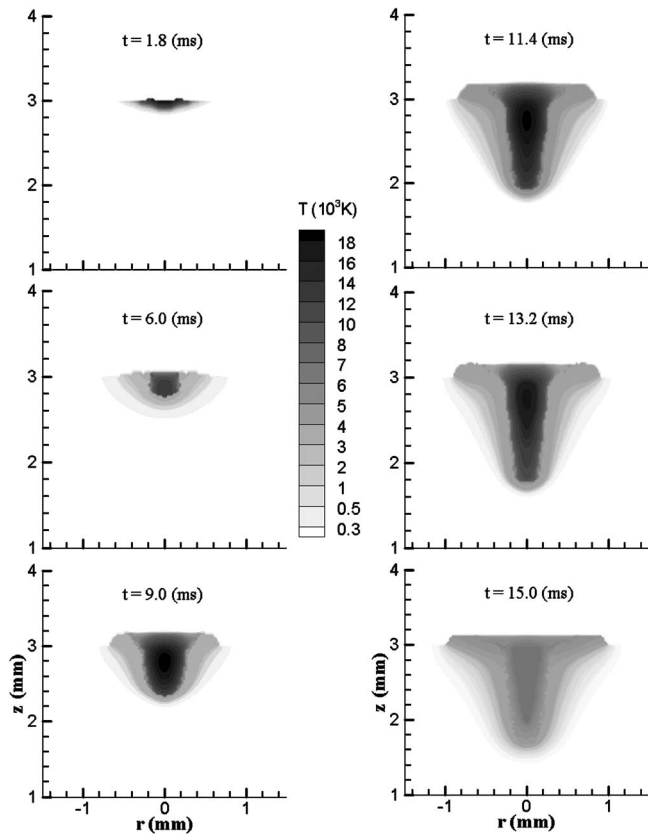
mechanism. A large amount of the laser energy is reflected back. Since the direction of the reflected light is contrary to its incident direction, this part of the laser light will never reach the weld pool surface again. However, once the keyhole is formed, the surface along the keyhole wall is not flat. Part of the reflected light will be incident on the keyhole wall again and again. During each incidence, part of the laser energy is absorbed via the Fresnel absorption mechanism. This brings more laser energy input to the keyhole wall, which leads to higher recoil pressure on the keyhole wall. Moreover, as the keyhole deepens, the possibilities and times of multiple reflections increase. When the reflected laser light travels in the plasma, part of its energy will also be absorbed by the plasma to increase the plasma temperature.

5.3 Fluid Flow and Weld Pool Dynamics. As shown in Fig. 4 at $t=1.8$ ms, since the weld pool is small and it takes time to accelerate the molten metal, the fluid flow is not significant. Once the keyhole is formed, with the strong action of the laser-induced recoil pressure, some strong velocities appear in the weld pool at $t=6.0$ ms. At $t=9.0$ ms, on the bottom of the keyhole wall, higher recoil pressure leaves a thinner liquid layer compared with that at $t=6.0$ ms. Although the hydrostatic pressure and surface tension at the bottom of the keyhole becomes larger and larger as keyhole deepens, which makes it difficult for the drilling process of the keyhole, the velocity of liquid along the bottom surface does not decrease, as shown in Fig. 4. Meanwhile, the hydrostatic pressure at the bottom of the keyhole increases as the keyhole deepens, which makes it more and more difficult for the recoil pressure to pump the liquid upwards. Moreover, the temperature difference along the sidewall of the keyhole decreases as the keyhole depth increases. This decreases the Marangoni shear stress and makes it more difficult for the squeezed liquid metal to flow upwards. As shown in Fig. 4, both the downward velocities at the bottom keyhole and the upward velocities along the sidewall of the keyhole
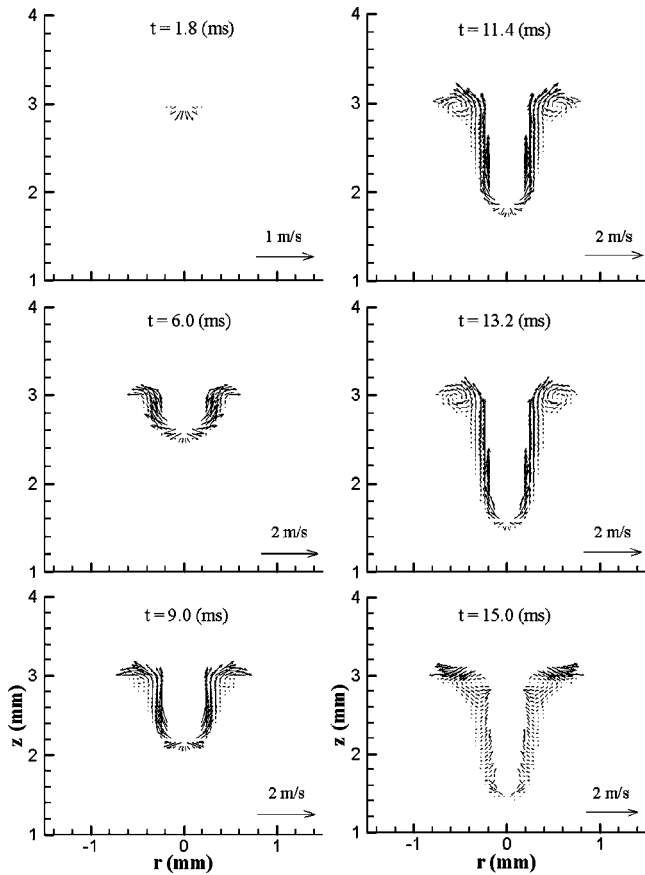
Fig. 4 The corresponding velocity distributions for the case shown in Fig. 2

Fig. 6 Coefficient of Inverse-Bremsstrahlung absorption as a function of plasma temperature from Ref. [16]

are smaller at $t=13.2$ ms compared with those at $t=11.4$ ms.

As shown in Fig. 7, the keyholing speed drops quickly after $t>10.5$ ms. This means more laser energy is absorbed by the keyhole plasma, especially by that in the upper part of the keyhole. Thus, it makes the plasma at that portion reach a very high temperature, as shown in Fig. 3. This hot plasma also increases the heat input to the keyhole wall. Meanwhile, the multiple reflections also bring more and more energy to the sidewall of the keyhole as keyhole deepens. The increased heat input to the sidewall of key-
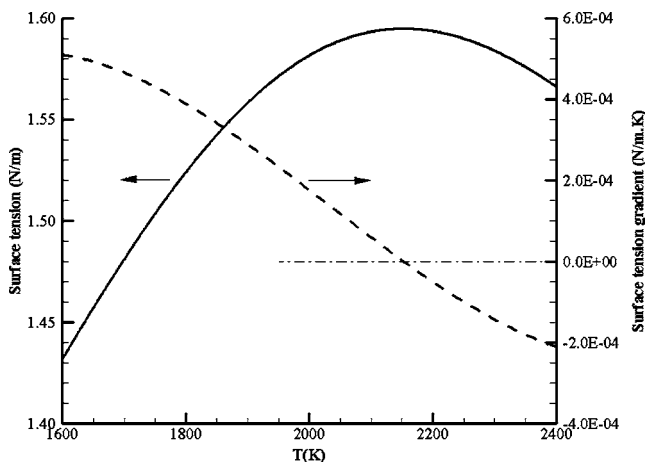
hole causes the liquid-solid interface in the keyhole to move outwards, which enlarges the heat affect zone in the weld substrate. Hence, as shown in Fig. 2, the liquid region of keyhole is enlarged at $t=15.0$ ms compared with that at $t=13.2$ ms and the keyhole depth does not increase remarkably at this period. Also, as noticed in the figure, the liquid metal on the bottom of the keyhole is thicker at $t=15.0$ ms than that at $t=13.2$ ms. This is because, with more and more laser energy being absorbed by the plasma, the recoil pressure on the bottom of the keyhole is decreasing at $t=15.0$ ms, hence more liquid metal is accumulated there.

As shown in Fig. 4, there is a vortex in the upper part of the weld pool at $t=13.2$ ms, which is the result of combined action of four driving forces: temperature-dependent Marangoni shear stress force, surface tension, hydrodynamic force, and hydrostatic force. On the upper part of the vortex, the liquid is driven from the hot edge to the cold edge by the Marangoni shear stress force when the temperature of liquid is above 2150 K. As the liquid metal moves to the cold edge, the temperature gradient becomes smaller and smaller which makes the Marangoni shear stress force decreases. At the point where the liquid temperature is under 2150 K, the Marangoni shear stress will change its direction. This change prevents the liquid from moving outwards. At the same time, the surface tension on the cold edge also blocks the liquid to flow outwards. Therefore, the velocity vector along the r direction

Fig. 5 Surface tension and its gradients as a function of temperature for the pseudo-binary Fe-S system with 300 ppm sulfur

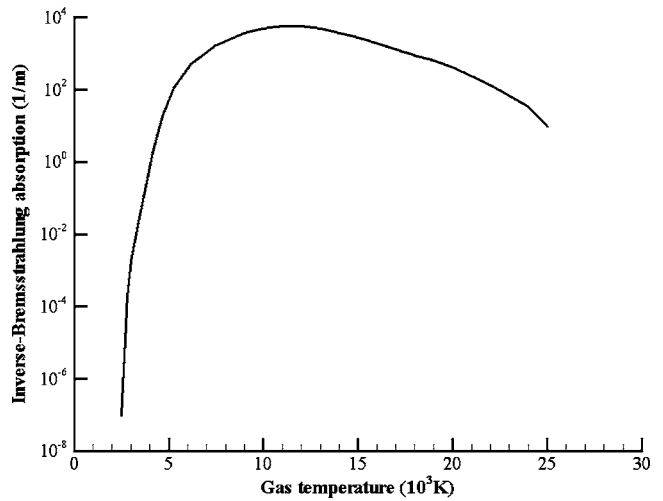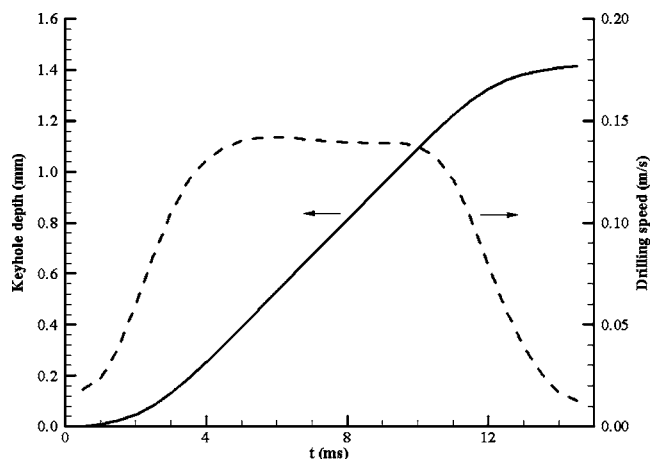**Fig. 7 Keyhole depth and keyholing speed as a function of time**
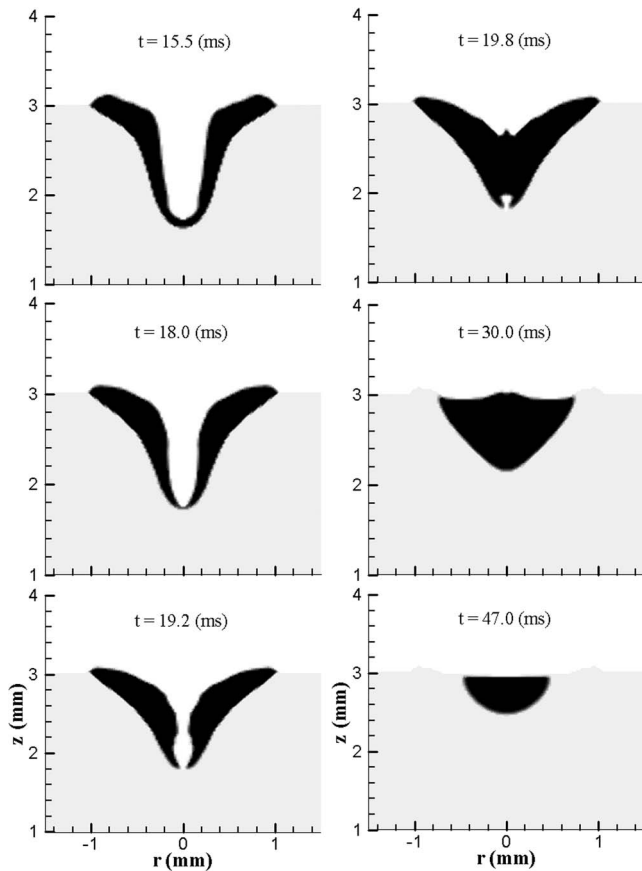
Fig. 8 A sequence of liquid metal evolution during the keyhole collapse and solidification processes

Fig. 9 The corresponding temperature distributions for the case shown in Fig. 8

becomes smaller and smaller. Meanwhile, the hydrostatic force and surface tension cause the liquid to flow downwards, which makes the velocity along the z direction become larger and larger. Finally, the liquid metal changes its flow direction to flow downwards at the upper of the cold edge. When this downward-flowing liquid metal meets the liquid-solid interface, it is blocked by this interface and flows along the interface. Meanwhile, the hydrodynamic force of the squeezed liquid from the lower part of keyhole makes the liquid flow upwards. Thus, the liquid changes its direction to flow upwards at the lower part of hot edge. As the liquid flows upwards, the hydrodynamic force is counteracted by the hydrostatic force and surface tension, which retards the upward tendency. Meanwhile, the Marangoni shear stress force pushes the liquid to flow toward the cold edge. Thus, the liquid flow rotates clockwise on the shoulder of keyhole and a vortex is formed as shown in the figure. The flow velocity is on the order of 10 cm/s, which agrees fairly well with the experimental results [11]. This vortex enhances the heat transfer along the liquid-solid interface and enlarges the liquid region on shoulder of the keyhole, as shown in Fig. 2.

5.4 Keyhole Collapse and Porosity Formation. When the laser pulse is shut off at $t=14.0$ ms, the recoil pressure disappears quickly and the keyhole collapses under hydrostatic pressure and surface tension. Figure 8 shows a sequence of the liquid metal evolution during the keyhole collapse and solidification processes. The corresponding temperature and velocity distributions are given in Figs. 9 and 10. Once the laser is shut off, the hot plasma radiation is the only heat input source for keyhole wall. However, since there is no heat input to the plasma and the heat capacity of plasma is very small, the temperature of the plasma drops very quickly. Meanwhile, the heat conduction from the keyhole wall to
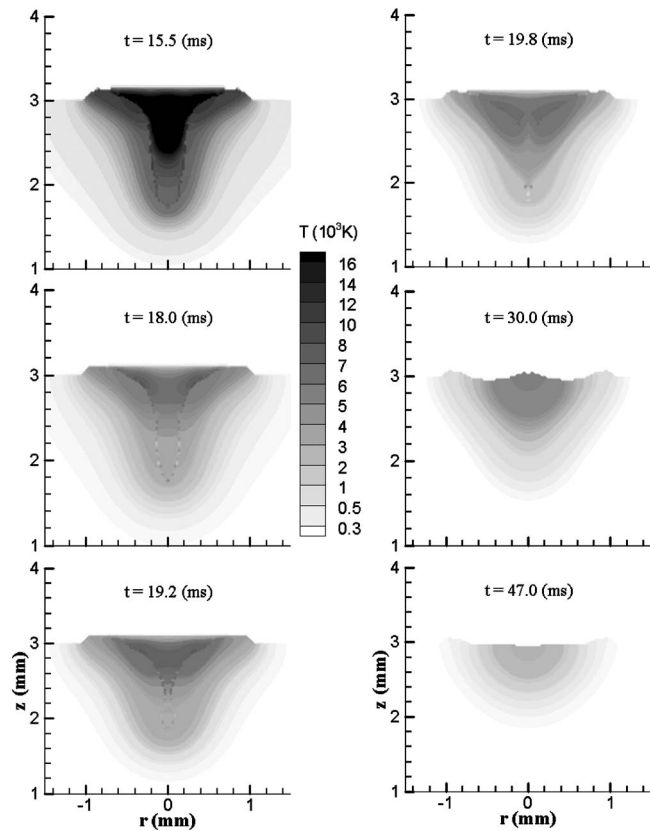
the surrounding metal is very strong due to the high aspect ratio and high temperature gradient. Hence, as shown in Fig. 9, the temperature of the keyhole wall drops very quickly, especially in the lower part of the keyhole since there is only a thin layer of the metal liquid. Due to this quick temperature drop, the thin layer of liquid metal on the bottom of keyhole completely solidifies at $t=19.2$ ms in Fig. 9.

At the initial stage of the collapse, the temperature gradient along the sidewall surface of the keyhole is negative from the bottom to the top and the temperature of the liquid metal is above 2150 K. Thus, the Marangoni shear stress is still positive, which helps the liquid to flow upwards. Since the temperature of the metal on the bottom surface drops much faster than that on the upper surface, the Marangoni shear stress there decreases quickly. Meanwhile, the hydrodynamic pressure of the squeezed liquid metal also decreases very quickly due to the removal of recoil pressure. The surface tension and hydrostatic pressure then make the liquid metal have a tendency to fill back the keyhole. However, the velocity of liquid metal needs a time to change its direction, especially on the lower part of the keyhole wall due to their original high velocities inertia. On the keyhole shoulder, the Marangoni shear stress also decreases quickly with the decreasing temperature gradient. Hence, with the action of hydrostatic pressure and surface tension, the liquid metal on the upper part of the keyhole starts to flow inwards and downwards at $t=15.5$ ms in Fig. 10. Since there is certain amount of liquid metal there and the flow friction along the liquid-solid interface is larger for the thin liquid layer, the back-filling velocities of the liquid metal on the upper part will be accelerated more easily than those on the lower part of keyhole. Thus, the keyhole is closed on the top first as shown in Fig. 8. Meanwhile, the liquid metal continues to be accelerated by the hydrostatic force to flow downwards along the keyhole wall and finally the keyhole is refilled at $t=30.0$ ms. As
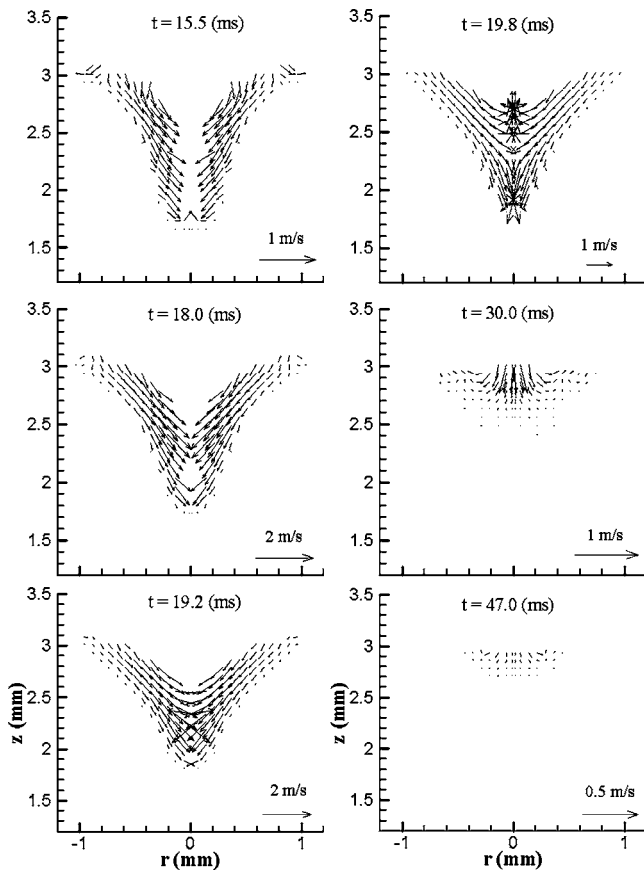
Fig. 10 The corresponding velocity distributions for the case shown in Fig. 8

Fig. 12 The comparison of the temperature history at location "A" between experimental result and model prediction

shown in Fig. 8 from $t=19.8$ ms to $t=30.0$ ms, the liquid region also shrinks as the liquid refills the keyhole, especially at the bottom because of fast conduction heat loss and low heat capacity. Finally, the liquid metal on the bottom completely solidifies. During the keyhole collapse process, the hot liquid metal cannot reach the far end of the top surface due to the disappearance of recoil pressure. Moreover, the velocity of the liquid metal flowing toward the edge decreases during the back-filling process. Thus, the liquid metal at the far end of the top surface cannot fill back and solidifies there, which results in a rough top surface on the final weld, as shown in Fig. 8 at $t=30.0$ ms.

5.5 Comparison Between Model Predictions and Experiments. To validate the numerical model, experiments were performed using the parameters listed before. In this study, the size and geometry of the weld bead are compared with simulated results in Fig. 11 and the temperature distribution comparisons are
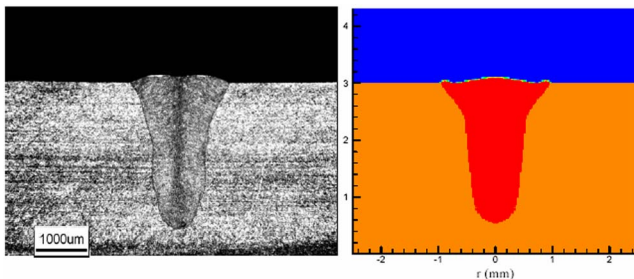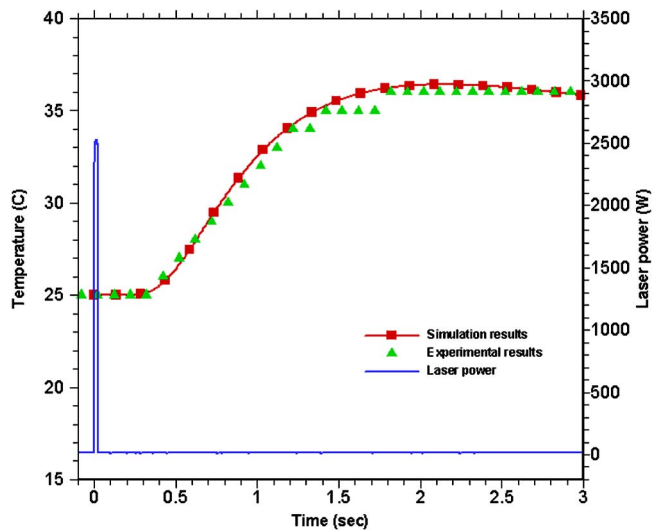
shown in Fig. 12. As shown in Fig. 11, when the laser power is 2.5 kW and the laser pulse duration is 20.0 ms, the penetration depth predicted by the model is 2.52 mm and it is 2.56 mm as shown in the experiment. The weld bead width is 1.96 mm from the model prediction and is 2.0 mm in the experiment. The top surface shape predicted by the model is slightly different from that shown in the experiment, and the size of the welded zone shown in the upper part of the welding coupon in the experiment is slightly larger than that predicted by the model. The difference between the model prediction and experimental results may be due to the difference of the input values of parameters (laser power, pulse duration, etc.) in the model and those in the experiments and the shielding gas effect. Overall, the weld bead geometry predicted by the model agrees well with that from the experiment. Also as shown in Fig. 12, the temperature history at location "A" predicted by the model agrees very well with that measured by the experiments. More comparison results are listed in Table 2 and, as shown, good agreements between experimental and computational results are obtained.

6 Conclusions

A mathematical model has been developed to simulate the transient keyhole formation, heat transfer, and fluid flow, and keyhole collapse process and the corresponding experiments were conducted to validate its efficiency. The model is divided into two submodels. One is to calculate the mass, momentum, and energy transport in the weld pool and the other is to calculate the energy transport in plasma. These two submodels provide boundary conditions for each other. The VOF technique is used to handle the free surface, and complicated velocity and temperature distributions are calculated.

Recoil pressure plays a key role in the keyhole formation, which pushes down the liquid in the weld pool and acts as the main driving force for the keyhole formation. This laser-induced recoil force combined with the Marangoni shear force, hydrodynamic force, and hydrostatic force causes very complicated fluid flow in the weld pool. A vortex is found at the upper part of keyhole, which is helpful in increasing the heat and mass transfer during the welding process.

Laser-induced plasma plays two-fold roles during keyhole formation. The positive effect is that the IB absorption increases the energy coupling, which facilitates the keyhole formation at the initial stage. The negative effect is that, when the keyhole reaches

Fig. 11 The comparison of the weld bead geometry between experimental result and model prediction

Table 2 Comparison of weld bead size between model predictions and experiment results

Laser Power (On-time) (kW)	Penetration (mm)		Width (mm)	
	Experiment	Calculated	Experiment	Calculated
1.8 (10.0 ms)	1.22	1.18	1.12	1.20
1.8 (20.0 ms)	2.01	2.04	1.74	1.82
1.8 (60.0 ms)	1.98	2.08	1.94	1.82
2.5 (20.0 ms)	2.56	2.52	2.00	1.96

certain depth, more laser energy is absorbed by the plasma and less laser energy could reach the keyhole wall, which prevents the keyhole from deepening further. Multiple reflections can bring more laser energy inside the keyhole to help the keyhole formation process.

During the keyhole collapse process, the keyhole closes on the top first and the liquid metal from the top then flows downwards to refill the keyhole. Porosity could be introduced during the keyhole collapse. Its formation is dependent on two factors: (1) solidification rate after the shut-off of the laser power and (2) backfilling speed of the liquid metal. The detailed discussion can be found in the forthcoming papers. The liquid metal on the far end of top surface cannot flow back in the solidification process, which results in a rough surface on the final weld. The temperature history and geometry of the weld bead predicted by the proposed model agree very well with the experimental results, which indicate the proposed mathematical model can be used as a solid base for future studies.

Acknowledgment

Nomenclature

A = constant in Eq. (11)
A_v = constant in Eq. (23)
B_0 = vaporization constant in Eq. (11)
c_p = specific heat
C = coefficient defined in Eq. (3)
d = dendrite arm spacing
E_i = ionization potential for neutral atom
f = mass fraction
f^α = sulfur concentration
F = volume of fluid function
F_{vis} = viscous energy dissipation
g = gravitational acceleration
g_e = degeneracy factor of electron particle
g_i = degeneracy factor of ion particle
g_0 = degeneracy factor of neutral atom
h = enthalpy for metal zone simulation
h_{pl} = enthalpy for plasma
h_c = convective heat-transfer coefficient
H = latent heat of fusion
H_v = latent heat for liquid-vapor
H_b = thickness of base metal
I = laser intensity
I_r = laser intensity leaving keyhole
k = thermal conductivity
K = permeability function in Eq. (2)
K_{pl} = plasma laser absorption coefficient
k_i = thermal conductivity for component i
k_B = Boltzmann's constant
M_a = atomic mass
m = times of reflection
m_e = electron mass

n = vector normal to local free surface
I = vector along the radiation direction
n_e = electron particle density in plasma
n_i = ion particle density in plasma
n_0 = neutral atom density in plasma
N_A = Avogadro's number
p = pressure for metal zone simulation
P_{atm} = atmospheric pressure
p_r = recoil pressure
p_σ = surface tension
q_{conv} = heat loss by convection
q_{evap} = heat loss by evaporation
q_{laser} = heat input flux by laser radiation
q_{radi} = heat loss by radiation
r-z = cylindrical coordinate system
r_f = laser beam radius
R = gas constant
R_b = radius of base metal
s = penetration depth of laser in plasma
s = vector tangential to local free surface
t = time
Δt = time step for metal zone simulation
Δt_{pl} = time step for plasma zone simulation
T = temperature
T_v = vaporization temperature
T_w = temperature on keyhole wall
u = velocity in the r direction
v = velocity in the z direction
V = velocity vector
V_I = ionization voltage
W = melt evaporation rate

Greek symbols

α_{pl} = fraction of laser absorbed by plasma
α_{IB} = IB absorption coefficient
α_{Fr} = Fresnel absorption coefficient
α_{mr} = plasma absorption coefficient at mth reflection
α_I = degree of ionization
β_T = thermal expansion coefficient
γ = surface tension coefficient
$\partial\gamma/\partial T$ = surface tension temperature gradient
ε = surface radiation emissivity
κ = free surface curvature
μ_l = dynamic viscosity
σ = Stefan-Boltzmann constant
ρ = density

Subscripts

0 = initial value
c = original incident laser light
IB = inverse bremsstrahlung absorption
l = liquid phase
r = relative to solid velocity
(r,m) = mth reflected laser beam
pl = plasma
s = solid phase

References

[1] Semak, V. V., Hopkins, J. A., McCay, M. H., and McCay, T. D., 1994, "A Concept for a Hydrodynamic Model of Keyhole Formation and Support During Laser Welding," *Proc. ICALEO*, pp. 641–650, Oct. 17–20, Orlando, FL.

[2] Semak, V. V., Hopkins, J. A., McCay, M. H., and McCay, T. D., 1994, "Dynamics of Penetration Depth During Laser Welding," *Proc. ICALEO*, pp. 17–20, Oct. 17–20, Orlando, FL.

[3] Hopkins, J. A., McCay, T. D., McCay, M. H., and Eraslan, A., 1993, "Transient Predictions of CO_2 Laser Spot Welds in Inconel 718," *Proc. ICALEO*, pp. 24–28, Oct. 24–28, Orlando, FL.

[4] Klemens, P. G., 1976, Heat Balance and Flow Conditions for Electron Beam and Laser Welding, J. Appl. Phys., **47**, pp. 2165–2174.

[5] Allmen, M., and Blatter, A., 1995, *Laser-Beam Interaction with Material*, 2nd ed., Springer-Verlag, Berlin.

[6] Solana, P., Kapadia, P., and Dowden, J., 1998, "Surface Depression and Ablation for a Weld Pool in Material Processing: a Mathematical Model," *Proc. ICALEO*, Sec. F, pp. 142–147, Nov. 16–19, Orlando, FL.

[7] Clucas, A., Ducharme, R., Kapadia, P., Dowden, J., and Steen, W., 1998, "A Mathematical Model of Laser Keyhole Welding Using a Pressure and Energy Balance at the Keyhole Walls," *Proc. ICALEO*, Sec. F, pp. 123–131, Nov. 16–19, Orlando, FL.

[8] Matsunawa, A., Kim, J., Seto, N., Mizutani, M., and Katayama, S., 1998, "Dynamic of Keyhole and Molten Pool in Laser Welding," J. Laser Appl., **10**, pp. 247–254.

[9] Chen, M. M., and Bos, J. A., 1998, "Melt Flow in Deep Penetration Welding," *Proc. ICALEO*, Sec. F, pp. 187–196, Nov. 16–19, Orlando, FL.

[10] Ducharme, R., Williams, K., Kapadia, P., Dowden, J., Steen, B., and Glowacki, M., 1994, "The Laser Welding of Thin Metal Sheets: an Integrated Keyhole and Weld Pool Model With Supporting Experiments," J. Phys. D, **27**, pp. 1619–1627.

[11] Sudnik, R., Rada, D., Breitschwerdt, S., and Erofeew, W., 2000, "Numerical Simulation of Weld Pool Geometry in Laser Beam Welding," J. Phys. D, **33**, pp. 662–671.

[12] Kapadia, P., Dowden, J., and Ducharme, R., 1996, "A Mathematical Model of Ablation in the Keyhole and Droplet Formation in the Plume in Deep Penetration Laser Welding," *Proc. ICALEO*, Sec. B, pp. 106–114, Oct. 14–17, Detroit, MI.

[13] Farson, D. F., and Kim, K. R., 1998, "Simulation of Laser Evaporation and Plume," *Proc. ICALEO*, Sec. F, pp. 197–206, Nov. 16–19, Orlando, FL.

[14] Miyamoto, I., Ohmura, E., and Maede, T., 1997, "Dynamic Behavior of Plume and Keyhole in CO_2 Laser Welding," *Proc. ICALEO*, Sec. G, pp. 210–218, Nov. 17–20, San Diego, CA.

[15] Solana, P., and Negro, G., 1997, "A Study of the Effect of Multiple Reflections on the Shape of the Keyhole in the Laser Processing of Material," J. Phys. D, **30**, pp. 3216–3222.

[16] Metzbower, E. A., 1997, "Absorption in the Keyhole," *Proc. ICALEO*, Sec. G, pp. 16–25, Nov. 17–20, San Diego, CA.

[17] Kothe, D. B., Mjolsness, R. C., and Torrey, M. D., 1991, "Ripple: A Computer Program for Incompressible Flows With Free Surfaces," LA-12007-MS, Los Alamos National Laboratory.

[18] Chiang, K. C., and Tsai, H. L., 1992, "Shrinkage-Induced Fluid Flow and Domain Change in Two-Dimensional Alloy Solidification," Int. J. Heat Mass Transfer, **35**, pp. 1763–1769.

[19] Dowden, J., Postacioglu, N., Davis, M., and Kapadia, P., 1987, J. Phys. D, **20**, pp. 36–44.

[20] Wang, Y., and Tsai, H. L., 2001, "Impingement of Filler Droplets and Weld Pool Dynamics During Gas Metal Arc Welding Process," Int. J. Heat Mass Transfer, **44**, pp. 2067–2080.

[21] Duley, W., 1999, *Laser Welding*, John Wiley & Sons Inc., New York.

[22] Sahoo, P., DeBroy, T., and Mcnallan, M. J., 1988, "Surface Tension of Binary Metal-Surface Active Solute Systems Under Conditions Relevant to Welding Metallurgy," Metall. Trans. B, **19**, pp. 483–491.

[23] Choo, R. T. C., Szekely, J., and David, S. A., 1992, "On the Calculation of the Free Surface Temperature of Gas-Tungsten-Arc Weld Pools From First Principles: Part II. Modeling the Weld Pool and Comparison With Experiments," Metall. Trans. B, **23**, pp. 371–384.

[24] Knight, C. J., 1979, "Theoretical Modeling of Rapid Surface Vaporization With Back Pressure," AIAA J., **17**, pp. 519–523.

[25] Semak, V., and Matsunawa, A., 1997, "The Role of Recoil Pressure in Energy Balance During Laser Materials Processing," J. Phys. D, **30**, pp. 2541–2552.

[26] Landau, L. D., and Lifshitz, E. M., 1980, *Statistical Physics*, 3rd ed., Pergamon, New York.

[27] Kaplan, A., 1994, "A Model of Deep Penetration Laser Welding Based on Calculation of the Keyhole Profile," J. Phys. D, **27**, pp. 1805–1814.

[28] Siegel, R., and Howell, J. R., 1992, *Thermal Radiation Heat Transfer*, 3rd ed., Hemisphere Publishing Corp., Washington, DC, Chap. 13.

[29] Ho, R., Grigoropoulos, C. P., and Humphrey, J. A. C., 1996, "Gas Dynamics and Radiation Heat Transfer in the Vapor Plume Produced by Pulsed Laser Irradiation of Aluminum," J. Appl. Phys., **79**, pp. 7205–7215.